# Supplementary information for

## Spin-polarized correlated insulator in monolayer $MoTe_{2-x}$

Zemin Pan[1#], Wenqi Xiong[1#], Jiaqi Dai[2,3#], Yunhua Wang[4], Tao Jian[1], Xingxia Cui[1], Jinghao Deng[1], Xiaoyu Lin[1], Zhengbo Cheng[1], Yusong Bai[1], Chao Zhu[1], Da Huo[1], Geng Li[5,6], Min Feng[1], Jun He[1,7], Wei Ji[2,3]*, Shengjun Yuan[1,7]*, Fengcheng Wu[1,7]*, Chendong Zhang[1,7]*, and Hong-Jun Gao[5]

[1]*School of Physics and Technology, Wuhan University, Wuhan 430072, China*
[2]*Beijing Key Laboratory of Optoelectronic Functional Materials & Micro-nano Devices, Department of Physics, Renmin University of China, Beijing 100872, China*
[3]*Key Laboratory of Quantum State Construction and Manipulation (Ministry of Education), Renmin University of China, Beijing, 100872, China*
[4]*Key Laboratory of Quantum Theory and Applications of Ministry of Education and School of Physical Science and Technology, Lanzhou University, Lanzhou 730000, China*
[5]*Beijing National Center for Condensed Matter Physics and Institute of Physics, Chinese Academy of Sciences, Beijing 100190, China*
[6]*Hefei National Laboratory, Hefei 230088, China*
[7]*Wuhan Institute of Quantum Technology, Wuhan 430206, China*

**Correspondence and request for materials should be addressed to:*
wji@ruc.edu.cn *(W.J.)*, s.yuan@whu.edu.cn *(S.J.Y)*, wufcheng@whu.edu.cn *(F.C.W)*, cdzhang@whu.edu.cn *(C.D.Z)*

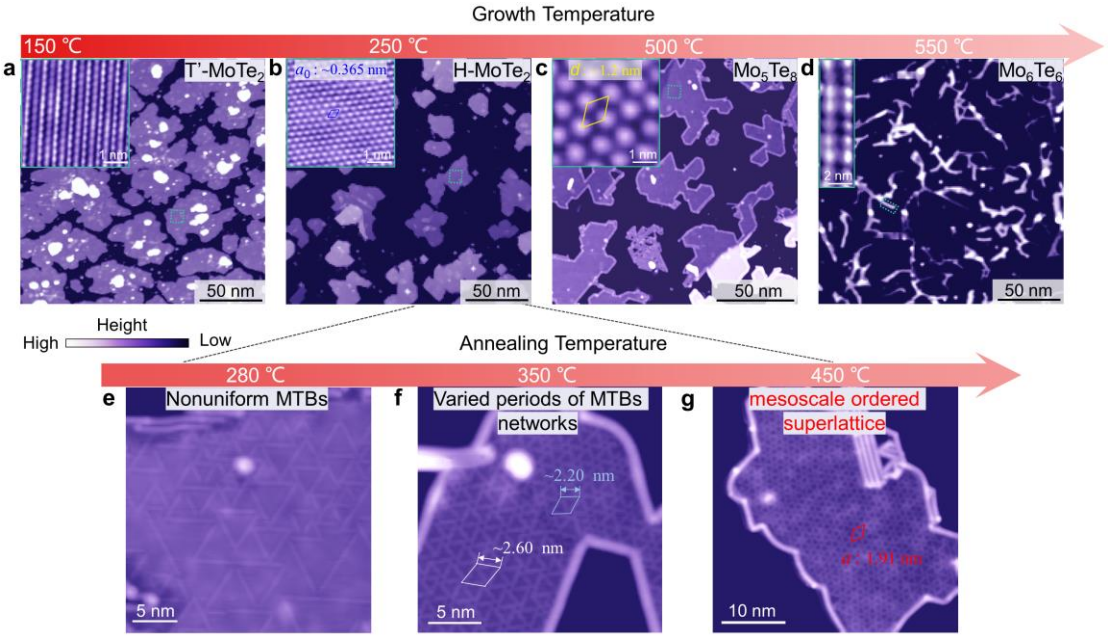


**Fig. S1. Phase control of monolayer (ML) Mo-Te compounds grown on BLG/SiC.** **a-d,** STM images of the sample growth at different substrate temperatures (during the depositions). The insets are zoomed-in images, illustrating the atomic structure of 1T'-$MoTe_2$ (**a**), the pristine 2H-$MoTe_2$ (**b**), and a $Mo_6Te_6$ bi-wire (**d**)[27-29]. The lattice constant $a_0$ of 2H-$MoTe_2$ is determined as 0.365 nm. The inset in (**c**) shows the typical superstructure of $Mo_5Te_8$[47] with a periodicity of $d \sim 1.2$ nm (yellow lines). For the H-$MoTe_2$ phase, we found the following annealing procedure can be exploited to engineer the concentration of mirror twin boundaries. With the increasing annealing temperature (annealing time is fixed as one hour), we see the evolution as illustrated in (**e-g**). With $T_{annealing}$ = 280 ºC, there are MTBs with random boundary lengths found on the surface. With $T_{annealing}$ = 350 ºC, the locally ordered networks start emerging. But various periodicities (two displayed here) coexist together with disordered regions. With $T_{annealing}$ = 450 ºC (**g**), one gets the ordered MTB superlattice with a uniform periodicity of 1.91 nm (marked by red lines). We emphasize that this superlattice is a thermally

favoured phase. In other words, a single-phase sample can be achieved with a large thermodynamic preparation window (as shown in Fig. 1a). Scanning parameters: (**a**-**c**) bias voltage $V_{bias}$ = 2 V; tunnelling current $I_t$ = 10 pA, inset (**a**) 5 mV, 100 pA, (**b**) -1 V, 50 pA, (**c**) -2 V, 20 pA, (**d**) 0.1 V, 200 pA, (**e**, **f**) 2 V, 20 pA, (**g**) 1 V, 20 pA.

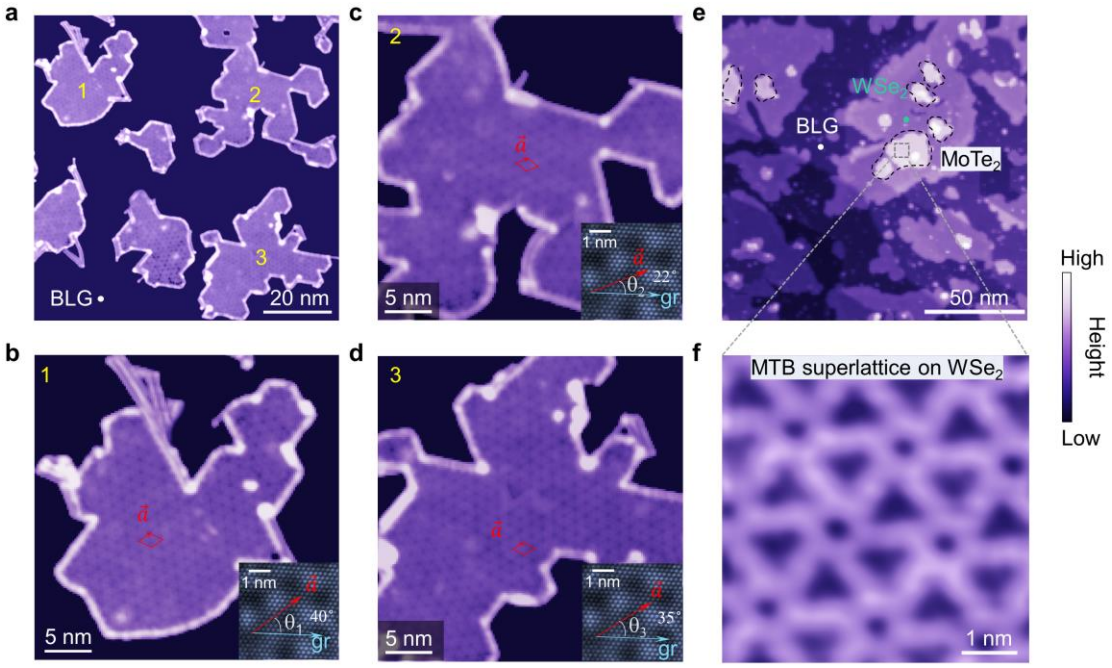


**Fig. S2. The evidence to rule out the possibility of a moiré pattern.** We note that some recent works identified the similar structure in $MoTe_2$ as a moiré pattern[29]. Here, we provide experimental evidence to rule out this possibility. **a,** A large-scale STM image of the ordered MTB superlattice. Three islands are marked as 1-3. (**b-d**) are close-up images of islands 1-3 with the supercell vectors ***a*** marked as shown. The insets in (**b-d**) are the atomically resolved images taken on the adjacent graphene. The blue arrows represent one zigzag direction of the graphene honeycomb. The twist angles between the MTB superlattice and the graphene atomic lattice can thus be determined as $\theta_1 \sim 40°$ (island 1), $\theta_2 \sim 22°$ (island 2), and $\theta_3 \sim 35°$ (island 3), respectively. **e,** Large-scale STM image of the ML-$MoTe_2$ grown on ML-$WSe_2$. Dashed black lines encircle the $MoTe_2$ islands. The growth parameters are the same as those of ML-$MoTe_2$ grown on graphene. (**f**) is the close-up image taken on $MoTe_2$/$WSe_2$ (corresponding to the grey square in (**e**)), exhibiting the same superstructures. These results prove the observed super periodicity (***a*** =1.91 nm) is independent of the twist angle and the

mismatch in lattice constants, and thus, cannot be a moiré pattern. Scanning parameters: (**a**-**d**) $V_{bias}$ = 1 V, $I_t$ = 50 pA. (**e**) 3 V, 10 pA. (**f**) 2 V, 50 pA.

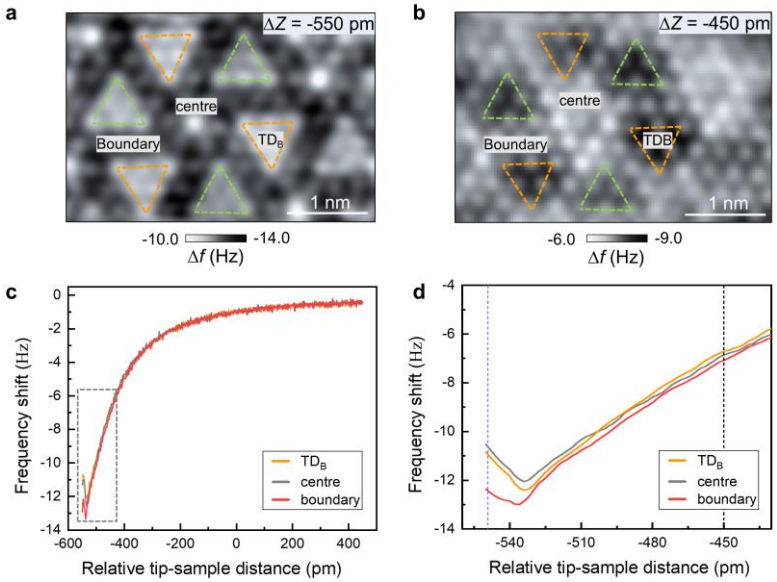


**Fig. S3. AFM image and force spectroscopic measurements. a, b,** Constant height $\Delta f$ images acquired on the MTB superlattice with different relative tip heights (as marked). **c,** Frequency shift as a function of tip-sample distance measured on the $TD_B$ (orange), the centre site (grey), and the boundary site (red). **d,** Zoomed-in spectra recorded at the grey dashed square in (**c**). The purple/black dashed vertical line in (**d**) corresponds to the ΔZ value used to acquire (**a**)/(**b**), respectively, illustrating the (**a**)/(**b**) was taken with repulsive/attractive force.

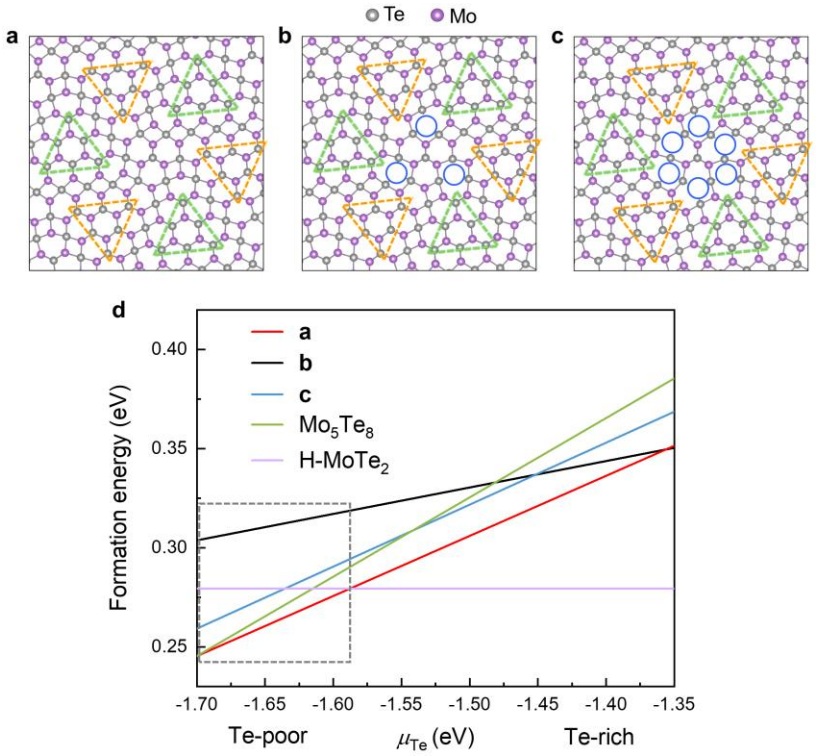


**Fig. S4. Formation energies of different Mo-Te compounds. a-c,** Three atomic models of the "wagon-wheel" structure. They are different in the number of Mo atoms missing near the centre region (indicated by blue circles). **a,** No Mo vacancies[31]; **b,** Three Mo vacancies[48]; **c,** Six Mo vacancies[30]. Since the scanning probe microscope (STM/AFM) only images the top layer atoms, one is not able to distinguish them through the atomically resolved imaging as shown in Figs. 1d and 1e. **d,** DFT calculated the formation energies of the following structures: model (**a**) (red line), model (**b**) (black line), model (**c**) (blue line), $Mo_5Te_8$ (green line), and pristine H-$MoTe_2$ (purple line). They are plotted as a function of Te chemical potential $\mu_{Te}$, simulating the uncertainty in experimental growth parameters (*i.e.*, the Te-poor and Te-rich conditions).

We found the pristine H-$MoTe_2$ is the most preferred structure at the Te-rich condition, while at the Te-poor condition (corresponding to the high-$T$ annealing in vacuum), the model (**a**) becomes more favoured than the pristine phase and the models

(**b**)/(**c**), as marked by the grey square in (**d**). With further reduction of $\mu_{Te}$, one can expect the formation energy of $Mo_5Te_8$ to be the lowest one. Our calculations well resemble the experimental results in Fig. S1. The validity of the atomic model (**a**) is also supported by the consistency in bias-dependent LDOS distribution between experiments and calculations, as shown in Fig. S5.

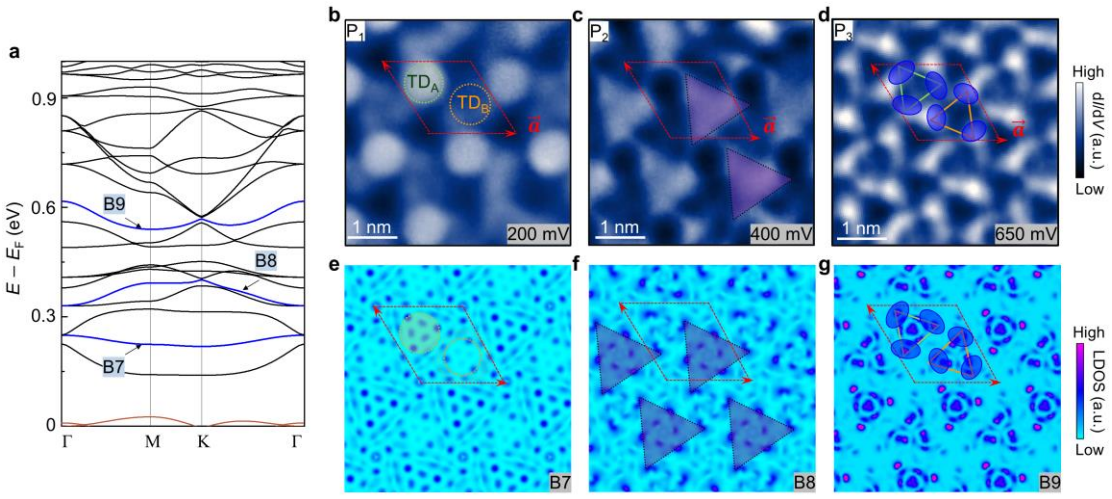


**Fig. S5. Spatial distributions of the electronic states at $P_1$, $P_2$, and $P_3$. a,** Calculated band structure in an energy window of 0 eV–1.0 eV (without spin polarization). Three bands (B7–B9) are highlighted in blue color. **b-d,** Measured d*I*/d*V* maps at the sample bias of 200 mV ($P_1$), 400 mV ($P_2$), and 650 mV ($P_3$). **e-g,** Calculated LDOS maps at the Γ points of B7, B8, and B9. Though a strict resemblance is hampered by the highly mixed band structures at these energy levels, the major experimental features are well captured in the simulations. For the P1 state, the LDOS is more concentrated in the $TD_A$ region than the $TD_B$ region (see **b** and **e)**. The contrast is reversed for the $P_2$ state. In **c** and **f**, one sees that the centre zone of the $TD_B$ contains a higher density than that of the $TD_A$, and a large triangular protrusion forms as marked by the purple shadow. In **d** and **g,** the electron states of $P_3$ are mostly distributed at the corners of each triangular domain (highlighted by the blue ovals), while the $TD_A$ centre is slightly higher than the $TD_B$ centre. The red rhombus in (**b**-**g**) labels a supercell. Stabilization parameters in (**b**), $I_t$ = 100 pA, lock-in modulation $V_{mod}$ = 4 mV; (**c**) 100 pA, 6 mV; (**d**) 100 pA, 8 mV.

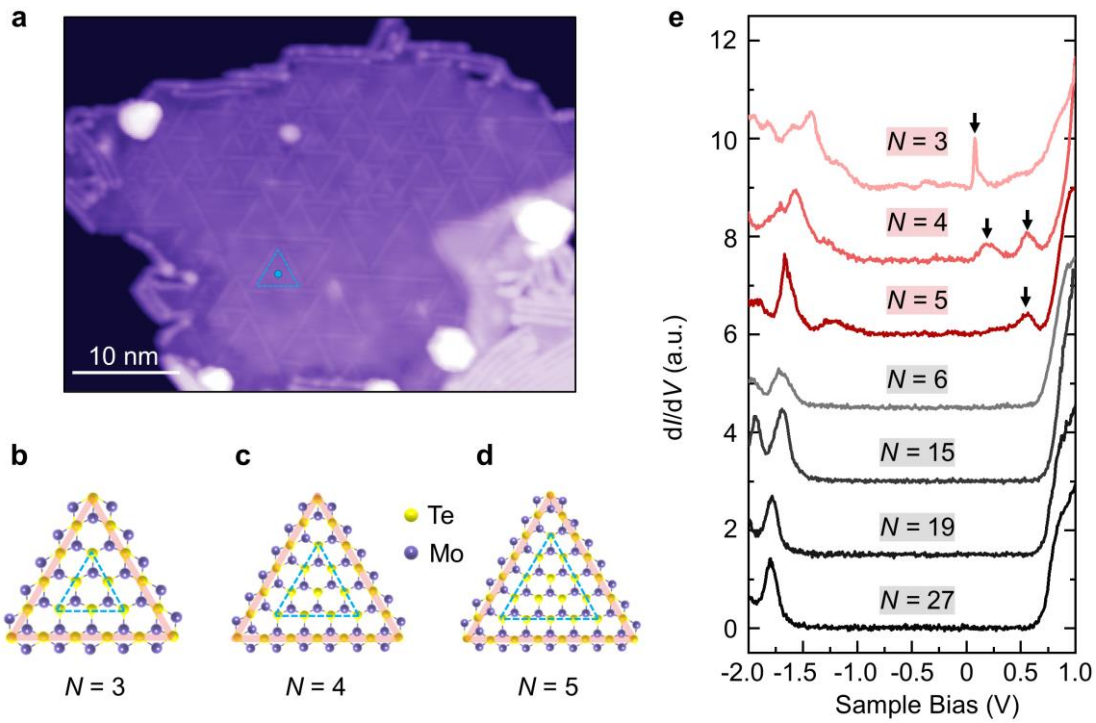


**Fig. S6. Size-dependent electronic properties of the triangular domains enclosed by MTB loops. a,** An STM image illustrating that the MTB loops enclosed triangular domains with varied sizes can be found on a sample annealed with relatively low temperature (Fig. S1e). **b-d,** The atomic models of the triangular domains with different sizes at $N = 3$, 4, and 5. Here, $N$ denotes the number of Te atoms at the domain (*i.e.*, the blue triangles) edges. To guide the eye, the Te rows in the middle of the boundaries are highlighted in red. **e,** d$I$/d$V$ spectra recorded at the centre of the blue triangular domains with different $N$ numbers (indicated by the blue dot in **a**). This illustrates how the localized 1D boundary states gradually extend into the inner domain with the shrinking of the domain size, and the threshold size of a triangular domain to have entirely extended in-gap states (black arrows) was $N = 5$. Noted that the spectra here were taken at locations without the formation of long-range ordered super periodicity. Thus, the line shape for $N = 3$ in (**e**) might be different from the ones shown in the main text.

Scanning parameters: (**a**) $V_{bias}$ = 2 V, $I_t$ = 10 pA. (**e**) $V_{bias}$ = 1.0 V, $I_t$ = 100 pA, lock-in modulation $V_{mod}$ = 10 mV.

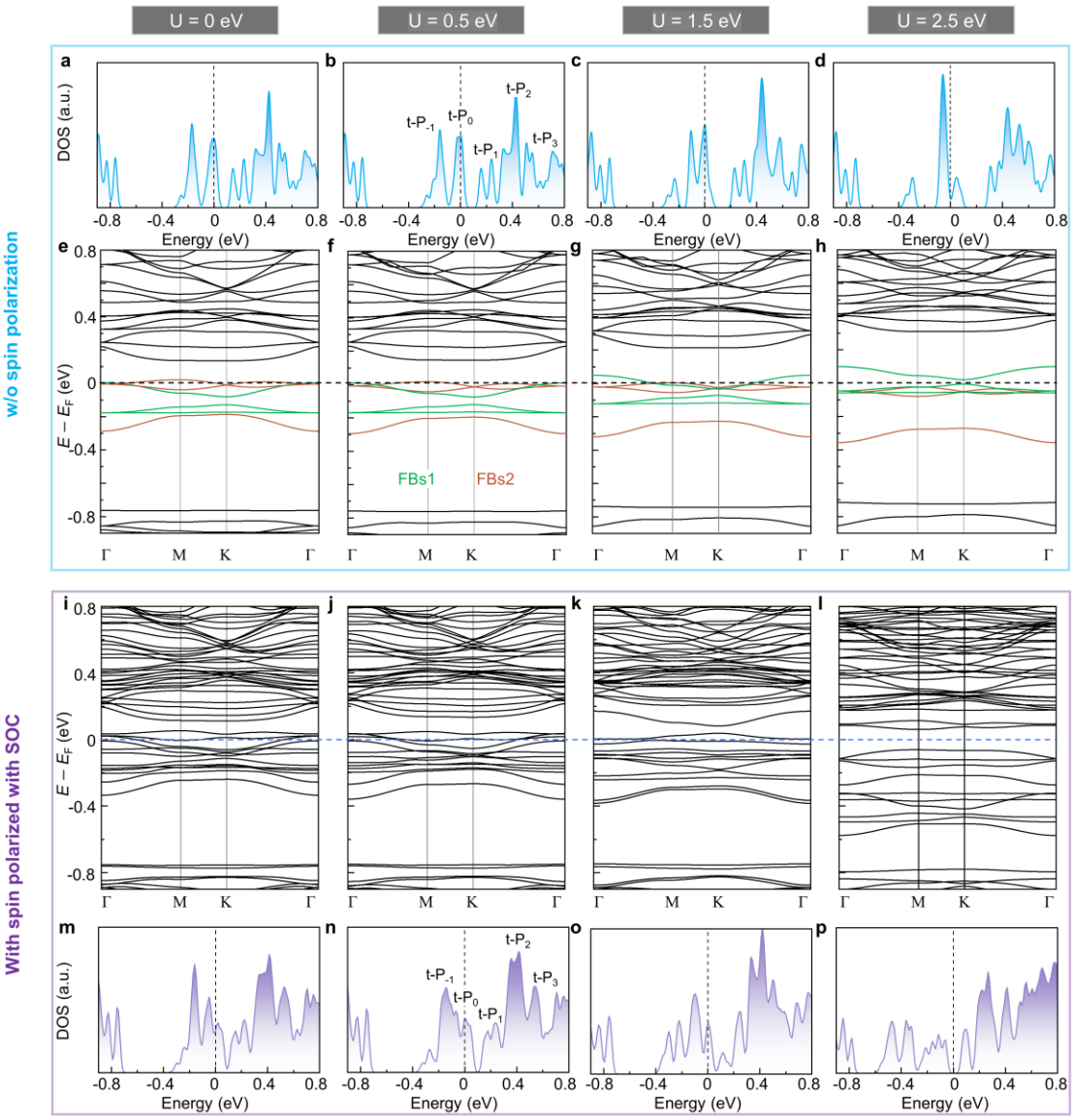


**Fig. S7. Discussion for the on-site repulsion energy *U*.** In (**a-d**), we present the DOSs (without spin polarization and SOC) obtained with Hubbard $U = 0$, 0.5 eV, 1.5 eV, and 2.5 eV. Here, $U$ is applied to the individual atomic orbital. The corresponding band structures are displayed in (**e-h**). The spin-polarized calculations (with SOC) are shown in (**i-p**).

The empty states majorly derive from highly mixed multiple bands. Thus, changes in the density of empty states with the increase of $U$ are somewhat vague (particularly when the spin polarization was involved), and it is hard to make a conclusive

comparison with the experimental data. On the occupied side, the DOS (corresponding to B1-B6) shows rather distinct changes with the raising of *U*. A significant effect of *U* on the B1-B6 is to shift the FBs1 upwards and the FBs2 downwards. Therefore, when $U > 0.5$ eV, pronounced DOS intensity will emerge below -0.2 eV. At $U = 2.5$ eV, sharp peaks are present at -0.5 eV, and the gap between the B1/6 states, and the onset of the bands continuum (~ -0.73 eV) is reduced to about 0.1 eV. These are significantly contrary to the experimental facts in Fig. 2a, where a flat and featureless line shape was observed within the range of -0.75 eV to -0.2 eV. Therefore, we conclude that a relatively small value of *U* is sufficient for our system. This assessment agrees with some recent studies of Mo-Te compounds[49,50]. The calculated results with $U = 0.5$ eV (**b** and **n**) give the best agreement with the spectroscopic line shape except for the zero-bias dip.

We note that with a satisfying agreement in the overall DOS (*i.e.*, a small *U*), the DFT+*U* calculation cannot reproduce the gap opening at the Fermi level. Only when the *U* is sufficiently large, one can find a gap opening in the spin-polarized calculations (panel **p**). However, the calculated DOS profile now deviates from the experimental one. The difficulty in DFT+*U* to comprehensively reproduce all experimental characters implies that a more complex model for *e-e* interactions beyond the on-site repulsion *U* on individual atomic orbitals (*e.g.*, long-range Coulomb interaction over the superlattice scale) needs to be considered for the observed correlated feature.

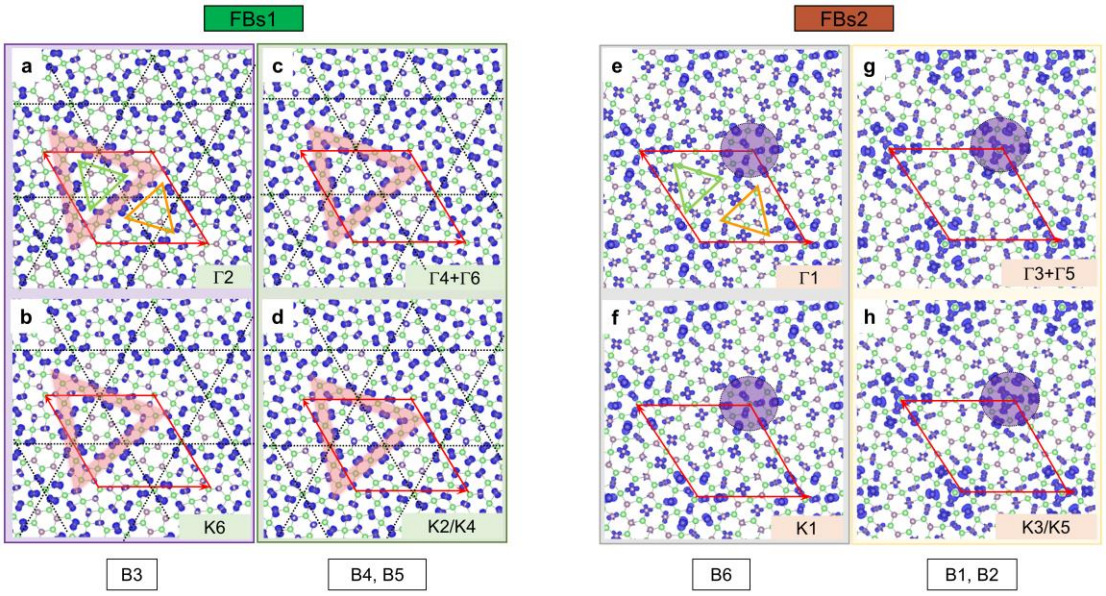


**Fig. S8. Calculated distributions of FBs1/2 states.** The spatial distributions at the "Γ4 + Γ6" (B4&B5 of FBs1) and "K3 + K5" (B1&B2 of FBs2) have been displayed in the main text as Figs. 2f and 2h. In (**a-d**), we show the calculated real-space distributions for all three bands in FBs1 at the Γ and K points, *e.g.*, Γ2 and K6 of the B3 band, Γ4 + Γ6 and K2 + K4 of the B4/5 bands. In (**e-h**), we show the distributions for FBs2, *e.g.*, Γ1 and K1 of the B6 band, Γ3 + Γ5, and K3/K5 of the B1/2 bands. All panels from the FBs1 exhibit a similar behavior that the boundary regions (highlighted by the pink triangles) have the most significant distribution of electronic states. The centres of the boundaries form a kagome lattice, akin to the line graph of a honeycomb lattice[35]. All panels from the FBs2 show that the states are majorly from the centre sites. The green (orange) triangles represent the $TD_{A\,(B)}$ regions, and the red rhombus labels a supercell.

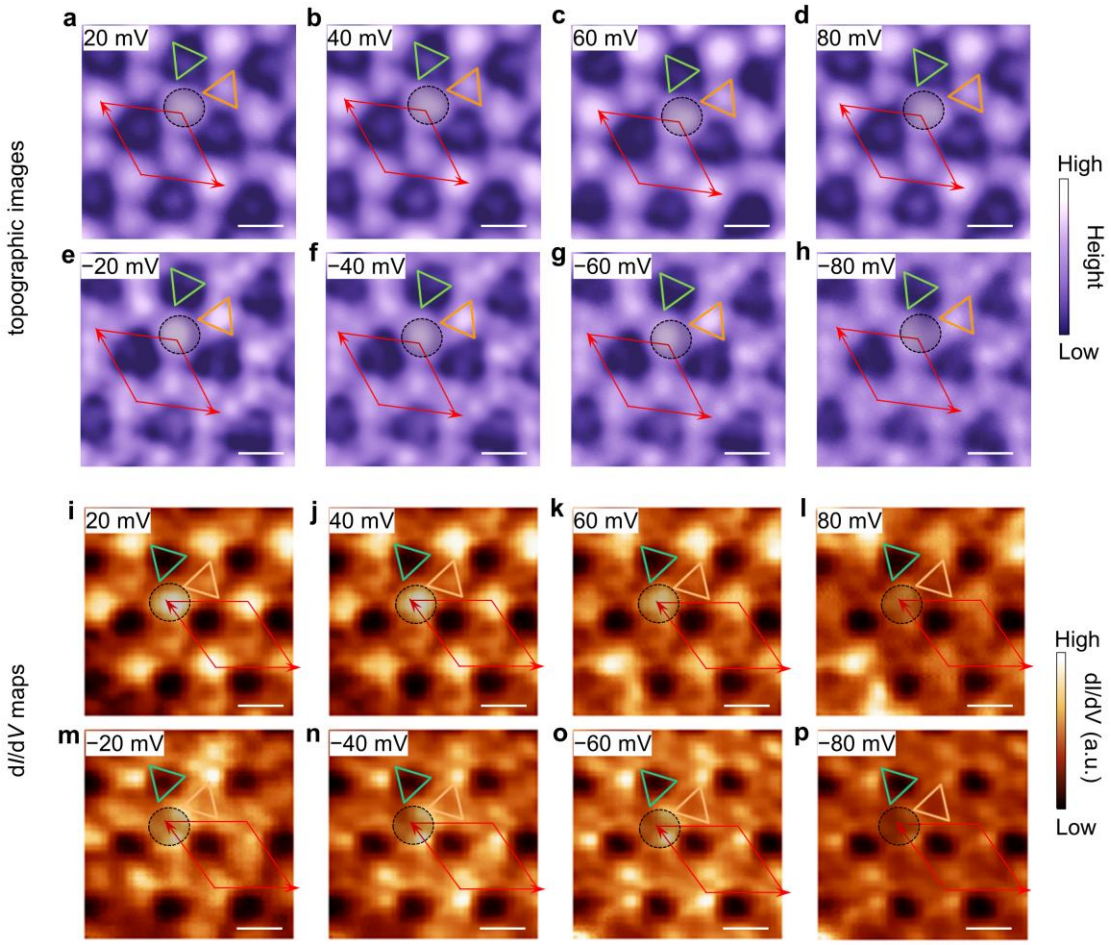


**Fig. S9. Bias-dependent STM imaging within an energy window around the $E_F$.** (**a-h**) are STM topographic images measured at the sample bias of ±20 mV, ± 40mV, ±60 mV, and ±80 mV. (**i-p**) are the corresponding differential conductance maps. These images were taken near the edges of the observed gap. No appearance of charge modulations can be identified beyond the original periodicity of the atomic structure. Moreover, the contrasts in both topographic and conductance images persist well when the sign of sample bias is reversed (*i.e.*, centre > $TD_B$ > $TD_A$). Thus, the most typical characteristic of a CDW gap, that the charge intensity reversal between the electron and hole[51,52], is not seen in our system. The red rhombus labels a supercell. Scale bars are 1

nm. Scanning parameters in (**a-h**), $I_t$ = 20 pA. Stabilization parameters in (**i-p**), $I_t$ = 100 pA, lock-in modulation $V_{mod}$ = 1 mV.

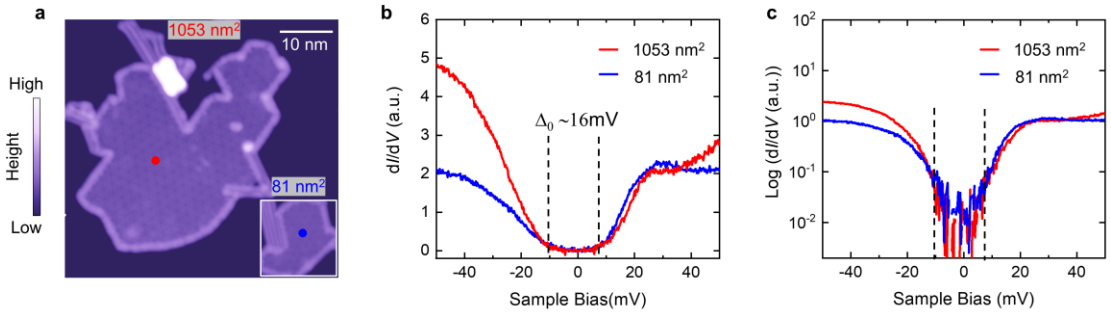


**Fig. S10. The gap width is regardless of the ML flake size.** We show the tunnelling spectra taken on two islands (**a**) with significant differences in the area (1053 $nm^2$ *vs.* 81 $nm^2$). **b** and **c** are the plots on linear and logarithmic scales, respectively. Almost identical gap widths ($\Delta_0 \sim 16$ mV) were observed. The absence of a correlation between gap width and island size contradicts the picture of the Coulomb gap[53-55] or the dynamic Coulomb blockade gap[56]. In addition, the 2D Efros-Shklovskii (ES) model[57] depicts a suppression of DOS near $E_F$ (also called the 2D Coulomb gap in some literature[58]). The gap in this model is expected to be linear in energy (namely, a "V"-shaped gap), which is dissimilar to our observations. Scanning parameters in (**a**), $V_{bias}$ = 1 V, $I_t$ = 50 pA. Stabilization parameters in (**b**), $V_{bias}$ = 50 mV, $I_t$ = 100 pA, $V_{mod}$ = 1 mV.

**Supplementary Note 1 Thermal broadening simulation.**

To demonstrate that the temperature dependence of the gap is not just an effect of thermal broadening, we have performed a thermal broadening simulation

$$\frac{dI}{dV}(eV) \propto \int_{-\infty}^{\infty} \rho(E) \left( \frac{d}{dV} F(E - eV, T) \right) \mathrm{d}E$$

where $\rho(E)$ is the zero-temperature density of states and $F(E,T)$ is the Fermi distribution function. In our simulation, As the thermal broadening at 0.35 K is negligible, we took the spectrum taken at 0.35 K as $\rho(E)$. Then, the red curve in Fig. 3c was generated by using the $F$ ($E$, T) at $T$ = 20 K.

**Table S1**. The character table of Γ/K -little group in space group $P\bar{6}$ which is used to determine the irreducible representations (IRs) for the energy bands at Γ/K of the MTB superlattice in the IRVSP program[46]. This character table is obtained from Bilbao Crystallographic Server[59].

| **Symmetry operation** | **1** | **2** | **3** | **4** | **5** | **6** |
|---|---|---|---|---|---|---|
| Seitz symbol | $\{1\|t_1,t_2,t_3\}$ | $\{3^+_{001}\|0,0,0\}$ | $\{3^-_{001}\|0,0,0\}$ | $\{m_{001}\|0,0,0\}$ | $\{\bar{6}^-_{001}\|0,0,0\}$ | $\{\bar{6}^+_{001}\|0,0,0\}$ |
| Γ1/K1 | 1.00+0.00i | 1.00+0.00i | 1.00+0.00i | 1.00+0.00i | 1.00+0.00i | 1.00+0.00i |
| Γ2/K2 | 1.00+0.00i | 1.00+0.00i | 1.00+0.00i | -1.00+0.00i | -1.00+0.00i | -1.00+0.00i |
| Γ3/K3 | 1.00+0.00i | -0.50+0.87i | -0.50-0.87i | 1.00+0.00i | -0.50+0.87i | -0.50-0.87i |
| Γ4/K4 | 1.00+0.00i | -0.50+0.87i | -0.50-0.87i | -1.00+0.00i | 0.50-0.87i | 0.50+0.87i |
| Γ5/K5 | 1.00+0.00i | -0.50-0.87i | -0.50+0.87i | 1.00+0.00i | -0.50-0.87i | -0.50+0.87i |
| Γ6/K6 | 1.00+0.00i | -0.50-0.87i | -0.50+0.87i | -1.00+0.00i | 0.50+0.87i | 0.50-0.87i |
| Γ7/K7 | 1.00+0.00i | -1.00+0.00i | -1.00+0.00i | 0.00-1.00i | 0.00+1.00i | 0.00-1.00i |
| Γ8/K8 | 1.00+0.00i | -1.00+0.00i | -1.00+0.00i | 0.00+1.00i | 0.00-1.00i | 0.00+1.00i |
| Γ9/K9 | 1.00+0.00i | 0.50-0.87i | 0.50+0.87i | 0.00-1.00i | -0.87-0.50i | -0.87+0.50i |
| Γ10/K10 | 1.00+0.00i | 0.50-0.87i | 0.50+0.87i | 0.00+1.00i | 0.87+0.50i | 0.87-0.50i |
| Γ11/K11 | 1.00+0.00i | 0.50+0.87i | 0.50-0.87i | 0.00-1.00i | 0.87-0.50i | 0.87+0.50i |
| Γ12/K12 | 1.00+0.00i | 0.50+0.87i | 0.50-0.87i | 0.00+1.00i | -0.87+0.50i | -0.87-0.50i |

## References


47. Zhang, J. et al. Single-layer $Mo_5Te_8$ — A new polymorph of layered transition-metal chalcogenide. *2D Mater.* **8**, abbc60 (2020).
48. Ma, Y., et al., Angle resolved photoemission spectroscopy reveals spin charge separation in metallic $MoSe_2$ grain boundary. *Nat. Commun.* **8**, 14231. (2017).
49. Beaulieu, S. et al. Ultrafast dynamical Lifshitz transition. *Sci. Adv* **7**, eabd9275 (2021).
50. Ma, Y. et al. Electronic and magnetic properties of perfect, vacancy-doped, and nonmetal adsorbed $MoSe_2$, $MoTe_2$ and $WS_2$ monolayers. *Phys. Chem. Chem. Phys* **13**, 15546-15553 (2011).
51. Jiang, Y. X. et al. Unconventional chiral charge order in kagome superconductor $KV_3Sb_5$. *Nat. Mater.* **20**, 1353-1357 (2021).
52. Thomson, R. E., Burk, B., Zettl, A. & Clarke, J. Scanning tunneling microscopy of the charge-density-wave structure in 1T-$TaS_2$. *Phys. Rev. B: Condens. Matter* **49**, 16899-16916 (1994).
53. Kouwenhoven L P, Austing D G, Tarucha S. Few-electron quantum dots. *Rep. Prog. Phys.* **64** (6), 701 (2001).
54. Yuan, Y. et al. Observation of Coulomb gap and enhanced superconducting gap in nano-sized Pb islands grown on $SrTiO_3$*. *Chin. Phys. Lett.* **37** (1), 017402 (2020).
55. Ganguli, S. C., Van ˇ o, V., Kezilebieke, S., Lado, J. L. & Liljeroth, P. Confinement-engineered superconductor to correlated-insulator transition in a van der Waals monolayer. *Nano Lett.* **22**, 1845-1850 (2022).
56. Brun, C. et al. Dynamical Coulomb blockade observed in nanosized electrical contacts. *Phys. Rev. Lett.* **108**, 126802 (2012).
57. Butko, V. Y., DiTusa, J. F. & Adams, P. W. Coulomb gap: How a metal film becomes an insulator. *Phys. Rev. Lett.* **84**, 1543-1546 (2000).
58. Song, Y. H. et al. Observation of Coulomb gap in the quantum spin Hall candidate single-layer 1T'-$WTe_2$. *Nat. Commun.* **9**, 4071 (2018).
59. M. I. Aroyo, J. M. Perez-Mato, D. Orobengoa, E. Tasci, G. de la Flor, A. Kirov

“Crystallography online: Bilbao Crystallographic Server” Bulg. *Chem. Commun.* **43** (2), 183-197 (2011).